



OPEN Enhancing light efficiency in phase-only holograms via neural network

Balakiruthika Periyasamy, Heeseong Hwang & Daeho Yang

Artificial neural networks have emerged as powerful tools for hologram synthesis and reconstruction, offering improvements in both image quality and computational efficiency. In this work, we present ShuffleResnet, a neural phase encoding approach designed to address the limitations of the conventional double phase encoding method (DPM) used for phase-only spatial light modulators (SLMs). The proposed model, ShuffleResnet, significantly enhances light efficiency, achieving a 59% increase compared to the conventional DPM. Numerical simulation results further demonstrate that the proposed model improves reconstruction quality and effectively suppresses artifacts in the complex field. Additionally, the model encodes complex field holograms at 1920×1080 resolution with an average inference speed of 4.74 milliseconds per hologram. The enhanced reconstruction fidelity increased light efficiency and fast inference, suggesting strong potential for real-time holographic applications.

Holography is an optical technique that reconstructs the three-dimensional wavefront of an object by recording both amplitude and phase components of light waves^{1,2}. At the time of Gabor's invention, the practical implementation of holography was limited due to the absence of coherent light sources. The evolution of holography began with the invention of lasers, leading to advanced imaging and display applications³. Alternatively, computer-generated holography (CGH)^{4,5} synthesizes holograms using computational methods, enabling the creation of both real and virtual objects for dynamic holographic 3D displays^{6–8}. Due to this computational flexibility, CGH is a promising technology for applications in education, entertainment, and medical treatment, where interactive and high-resolution visualization is essential^{9,10}.

Spatial light modulators (SLMs) are key optical display devices used in holography for wavefront modulation. However, commercially available SLMs cannot perform complex field modulation, as they can only modulate amplitude or phase individually¹¹. Therefore, a complex hologram needs to be converted into an amplitude-only or phase-only hologram using encoding techniques¹². Compared to amplitude-only holograms, phase-only holograms offer higher diffraction efficiency and effectively suppress the conjugate image during reconstruction. However, amplitude control of the reconstructed image is challenging in phase-only holograms¹³.

Over the years, a variety of encoding methods have been proposed for phase-only holograms. Iterative methods, including the Gerchberg-Saxton (GS) algorithm^{14,15} and stochastic gradient descent (SGD)^{16–18} have demonstrated the capability to achieve high-quality reconstructed images. On the other hand, non-iterative methods, such as error diffusion and down-sampling techniques, were developed but often result in reduced image quality^{19–21}. Moreover, a hybrid technique²² based on the optimized random phase method was introduced, enabling rapid synthesis of phase-only holograms. Shi et al.^{23,24} introduced a deep learning approach that enables real-time phase-only hologram generation, significantly reducing computational complexity while improving reconstruction quality for holographic display applications.

The double phase encoding method (DPM) is an efficient and computationally fast technique for phase-only holograms. In DPM, both amplitude and phase are encoded into two-phase components²⁵ often arranged in a checkerboard pattern²⁶. Despite its advantages, the encoded holograms are affected by spatial artifacts due to the conversion of complex amplitude into a phase-only representation. To address these issues, the band-limited double phase method was developed, incorporating optical filtering²⁷ in the frequency domain to suppress high-frequency artifacts. Kim et al.²⁸ proposed a weight factor method to improve diffraction efficiency and suppress noise. In 2020, Sui et al.²⁹ introduced a spatiotemporal double phase hologram approach that reduces speckle noise. In 2023, Zhong et al.³⁰ proposed a real-time 4 K CGH generation based on encoding conventional neural network with learned layers, demonstrating effective 3D hologram generation at a single wavelength. In 2024, Yan et al.³¹ demonstrated a deep learning approach using full convolution neural networks for recoding double phase holograms, effectively suppressing fringe artifacts at the edges of the diffraction field.

However, due to the spatial artifacts and the filtering structure that blocks part of the light, the reconstruction image quality and optical efficiency of the conventional DPM remain limited. In this work, we enhance the light

Department of Physics, Gachon University, 1342 Seongnam-daero, Sujeong-gu, Seongnam-si, Gyeonggi-do, Korea. ✉email: sheepvs5@gachon.ac.kr

efficiency of phase-only holograms by using a neural network-based encoding method. The proposed model, ShuffleResnet, achieves a 59% improvement in light efficiency, maintains high reconstruction quality, and significantly reduces artifacts compared to the conventional DPM. To achieve this, we employ a combination of supervised and unsupervised loss functions, along with an efficiency term. Moreover, the proposed model encodes RGB 2 K CGHs within 4.74 milliseconds, offering both speed and efficiency suitable for real-time applications.

Conventional DPM

DPM is a widely used non-iterative method for encoding complex amplitude fields into phase-only holograms, using two phase values per pixel, enabling high image quality hologram reconstruction. To represent the complex field, $U(x, y)$, using only phase values, DPM decomposes the field into two phase terms²⁶.

$$U(x, y) = e^{i\theta_1} + e^{i\theta_2} \quad (1)$$

where the two-phase values of θ_1 and θ_2 are defined as:

$$\theta_1 = \phi + \arccos\left(\frac{A}{A_{max}}\right), \quad (2)$$

$$\theta_2 = \phi - \arccos\left(\frac{A}{A_{max}}\right). \quad (3)$$

To implement the encoding, the two phase values θ_1 and θ_2 are alternately arranged across the pixel array, creating a checkerboard pattern of the phase-only values³².

Figure 1 illustrates the conventional DPM of the complex field $U(x, y)$. The original complex field, represented in the left block, consists of individual cells, in which each cell of $U(x, y)$ has a complex number with both amplitude and phase components. The middle block shows the core of DPM, where the complex field is split into two phase components θ_1, θ_2 .

Training of neural network

Figure 2 presents the detailed training process of the neural network model. The proposed model consists of pixel shuffle and unshuffle operations combined with residual blocks, as explained in detail in the methods section. The model takes complex holograms as input, and its output corresponds to the phase encoded value. The training process employs a hybrid loss function, which combines both supervised (L_{DPM}) and unsupervised loss (L_r) along with an efficiency term, L_e . The supervised loss accelerates training, and the unsupervised loss is used to minimize the reconstruction error to enhance the reconstruction quality. The scaling ratios α, β, γ balance the contribution of each term during training, as further discussed in the hyperparameter tuning result section. As a result, the total loss function can be written as:

$$L = r_s(n) \alpha L_{DPM} + (1 - r_s(n)) (\beta (-L_e) + \gamma L_r). \quad (4)$$

L_{DPM} is calculated as:

$$L_{DPM} = \frac{1}{N} \sum_{x,y} \frac{1}{M} \sum_{i=1}^M [(Re(z_i)(x, y) - Re(t_i)(x, y))^2 + (Im(z_i)(x, y) - Im(t_i)(x, y))^2] \quad (5)$$

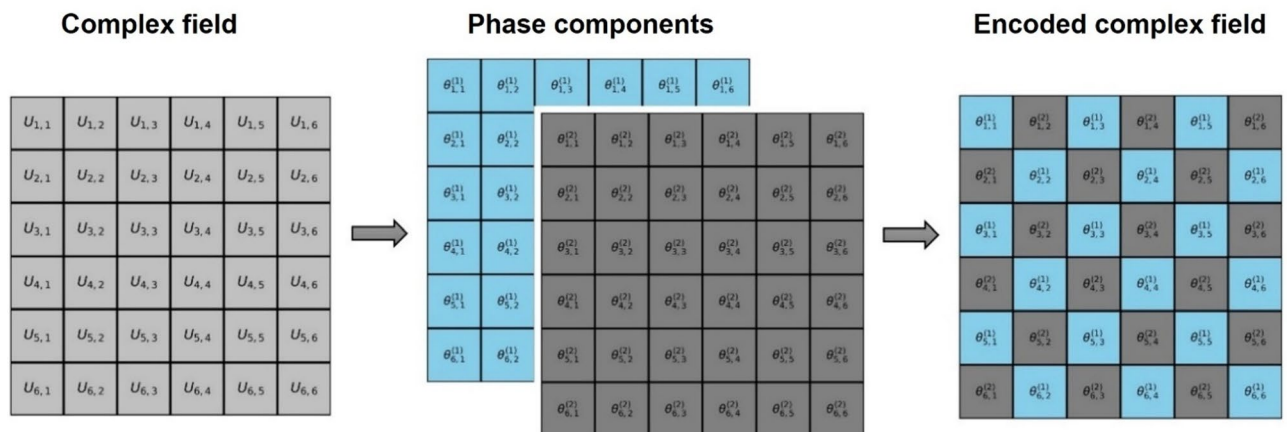


Fig. 1. Schematic of the conventional DPM. The first panel shows the original complex field, the middle panel illustrates the calculated phase components from the complex field, and the final panel shows the encoded complex field.

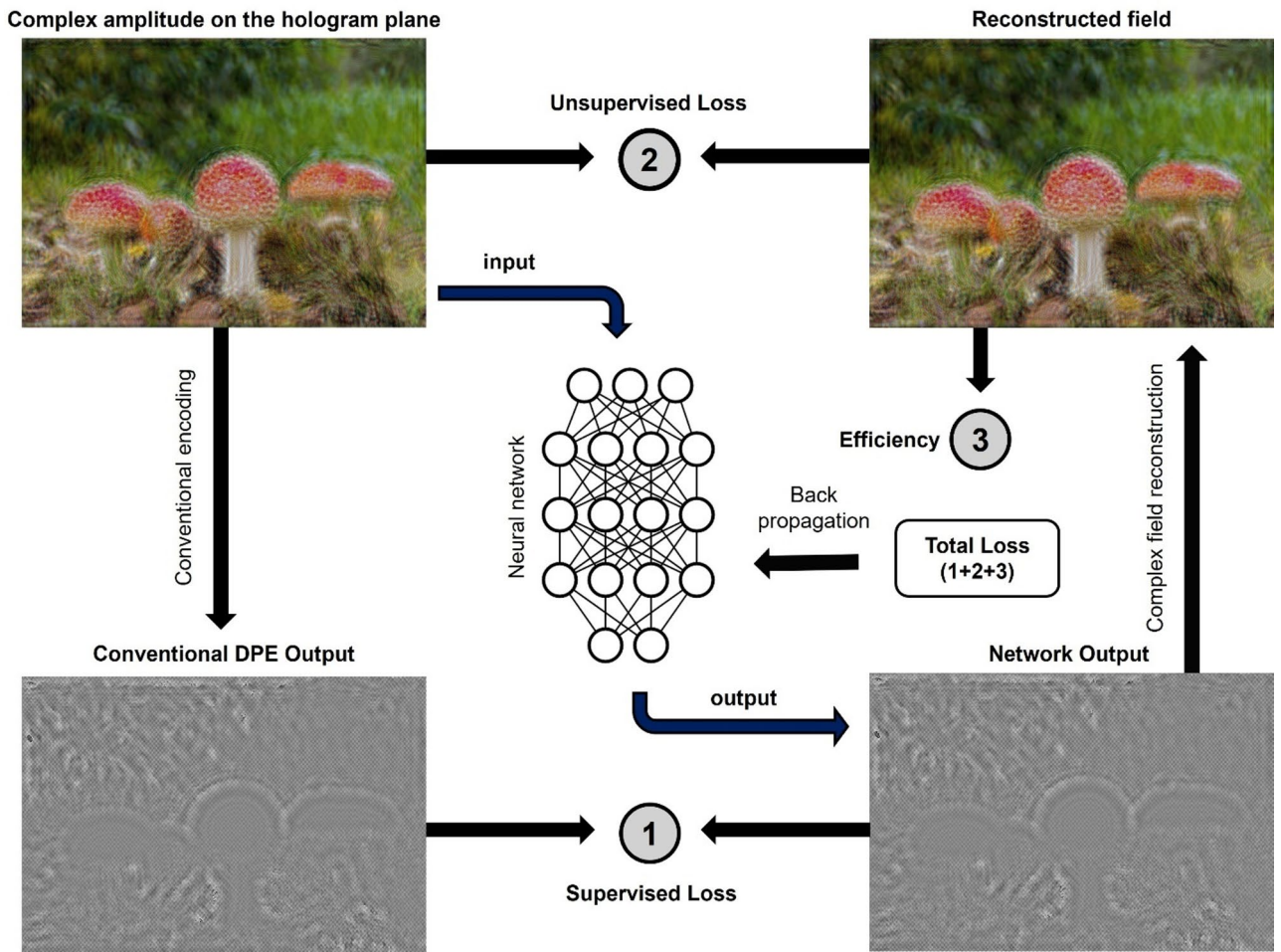


Fig. 2. Overview of the training scheme using a neural network for hologram encoding. The model takes a complex amplitude on the hologram plane as input and produces an encoded hologram as output. The hologram synthesized by the conventional DPM is used as the supervised target. The model output is numerically reconstructed and compared with the original input to compute the unsupervised reconstruction loss. Additionally, an efficiency term is used to evaluate the reconstruction quality. Finally, the total loss, which integrates all three loss terms, is backpropagated to optimize the network.

L_{DPM} is the mean squared error loss between the network output $z_i(x, y)$ and conventional DPM output $t_i(x, y)$ as target, calculated for both real and imaginary components. N is the number of holograms in one training batch. M is the number of pixels in each hologram.

L_r is computed as:

$$L_r = \frac{1}{N} \sum_{x,y} \frac{1}{M} \sum_{i=1}^M [(Re(c_i)(x, y) - Re(r_i)(x, y))^2 + (Im(c_i)(x, y) - Im(r_i)(x, y))^2] \quad (6)$$

L_r computes the mean squared error loss between the original complex field $c_i(x, y)$ and reconstructed complex field $r_i(x, y)$ for both real and imaginary components.

The light efficiency L_e is computed as:

$$L_e = \frac{1}{N} \sum_{x,y} |U_{recon}(x, y)|^2 \quad (7)$$

where $U_{recon}(x, y)$ is the reconstructed complex field, and N is the total number of pixels.

where $r_s(n)$ is the supervised ratio at epoch n , which determines the relative weight between supervised and unsupervised loss components. To ensure a smooth transition from supervised encoding to unsupervised encoding, we define $r_s(n)$ using exponential decay as, $r_s(n+1) = dr_s(n)$, where d is a decay constant. In other words, $r_s(n)$ can be expressed as:

$$r_s(n) = r_s(0) e^{dn} \quad (8)$$

where $r_s(0)$ is the initial supervised ratio set to 1. The exponential decay allows the model to initially learn from supervised double phase encoding targets and gradually rely more on unsupervised reconstruction and efficiency objectives as training progresses.

Figure 3 illustrates the training performance of ShuffleResnet and U-Net in terms of peak-signal-to-noise ratio (PSNR) and light efficiency across training epochs. In Fig. 3a, the reconstruction PSNR of ShuffleResnet increases steadily and reaches a peak value of approximately 32 dB. The stable PSNR indicates that the network learns a consistent and effective encoding strategy to improve reconstruction quality. In Fig. 3b, the reconstruction efficiency of ShuffleResnet shows a gradual increase after 10 epochs, eventually reaching a maximum value of approximately 0.42. The improved efficiency after ten epochs is due to the exponential decay of $r_s(n)$, which shifts the training focus from supervised encoding to optimizing reconstruction and efficiency. The enhanced efficiency reflects how effectively the input light is utilized in the reconstruction process.

For comparison, a U-Net model was trained under the same conditions, and its performance was evaluated along with ShuffleResnet in Fig. 3. Compared to ShuffleResnet, the U-Net model exhibits significantly lower PSNR and reduced light efficiency. During initial epochs, U-Net's light efficiency increases rapidly because the model initially learns the conventional DPM patterns using the supervised target. However, after epoch 10 when the supervised weight begins exponential decay, the model gradually shifts its focus toward the more challenging unsupervised reconstruction objective. After the transition, the model is no longer trained by DPM, but by a complex objective that optimizes both reconstruction quality and light efficiency. As a result, the measured light efficiency gradually declines to approximately 0.25 by the end of training, as shown in Fig. 3b. The comparison results confirm that ShuffleResnet performs better than U-Net.

Evaluation results

To evaluate the reconstruction performance of the proposed model, we compared the complex field reconstruction results of ShuffleResnet and conventional DPM. We used conventional DPM as our baseline because its output was used to generate the targets for our initial supervised training phase. The CGHs used in the validation assumed that the 2D floating hologram is 10 mm away from the SLM, where the 2D floating images are the DIV2K validation dataset. To synthesize the CGHs, the images were numerically propagated using the angular spectrum method (ASM). During the complex field reconstruction using the encoded output, a band-limiting optical filter was applied to suppress high-frequency diffraction noise. Although random propagation depths were used during training to improve generalization, a fixed depth was adopted to ensure consistent metric calculation.

Figure 4 presents the numerical complex field reconstruction results obtained using ShuffleResnet and the conventional DPM, compared against the target complex holograms. The figure displays the magnitude of the reconstructed complex fields for visual comparison, while the quantitative evaluation (PSNR and efficiency) is performed on the complete complex data including both real and imaginary components. In the numerical reconstructions, the ringing patterns and diffractions are visible, serving as indicators of depth. While the reconstructed output from ShuffleResnet is nearly identical to the target, the conventional method presents noticeable spatial artifacts. For instance, in Fig. 4j, there are speckles in the eye of the animal, whereas the corresponding output in Fig. 4f shows a clear view of the eye that closely matches the target. As a result, the reconstructed complex field outputs from ShuffleResnet achieve higher PSNR and improved light efficiency values compared to the conventional method.

Encoding results comparison

Figure 5 provides a visual and quantitative comparison of the encoded holograms and corresponding intensity reconstruction results from the proposed ShuffleResnet and conventional DPM. In Fig. 5a, the encoded output

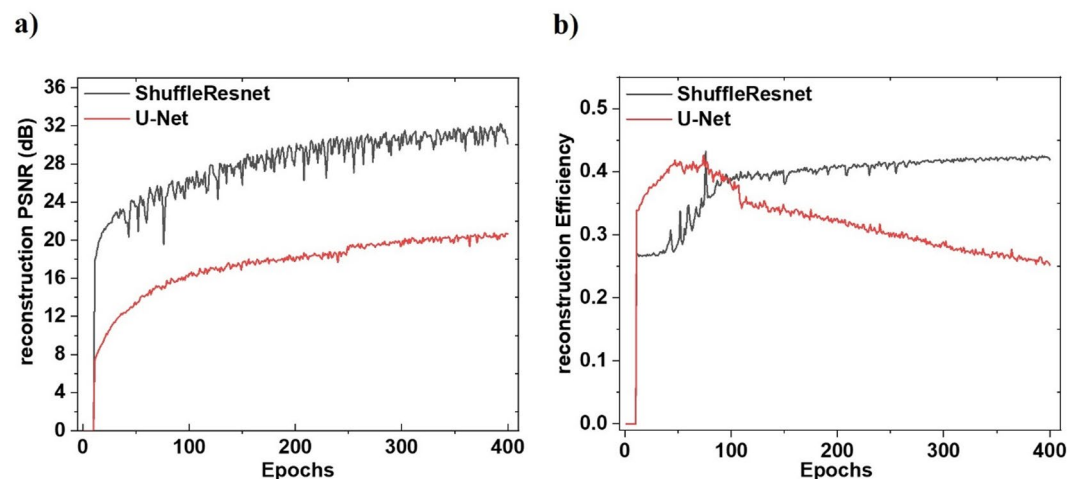


Fig. 3. Comparison of training performance between ShuffleResnet and U-Net. (a) Reconstruction PSNR. (b) Reconstruction efficiency as a function of training epochs.

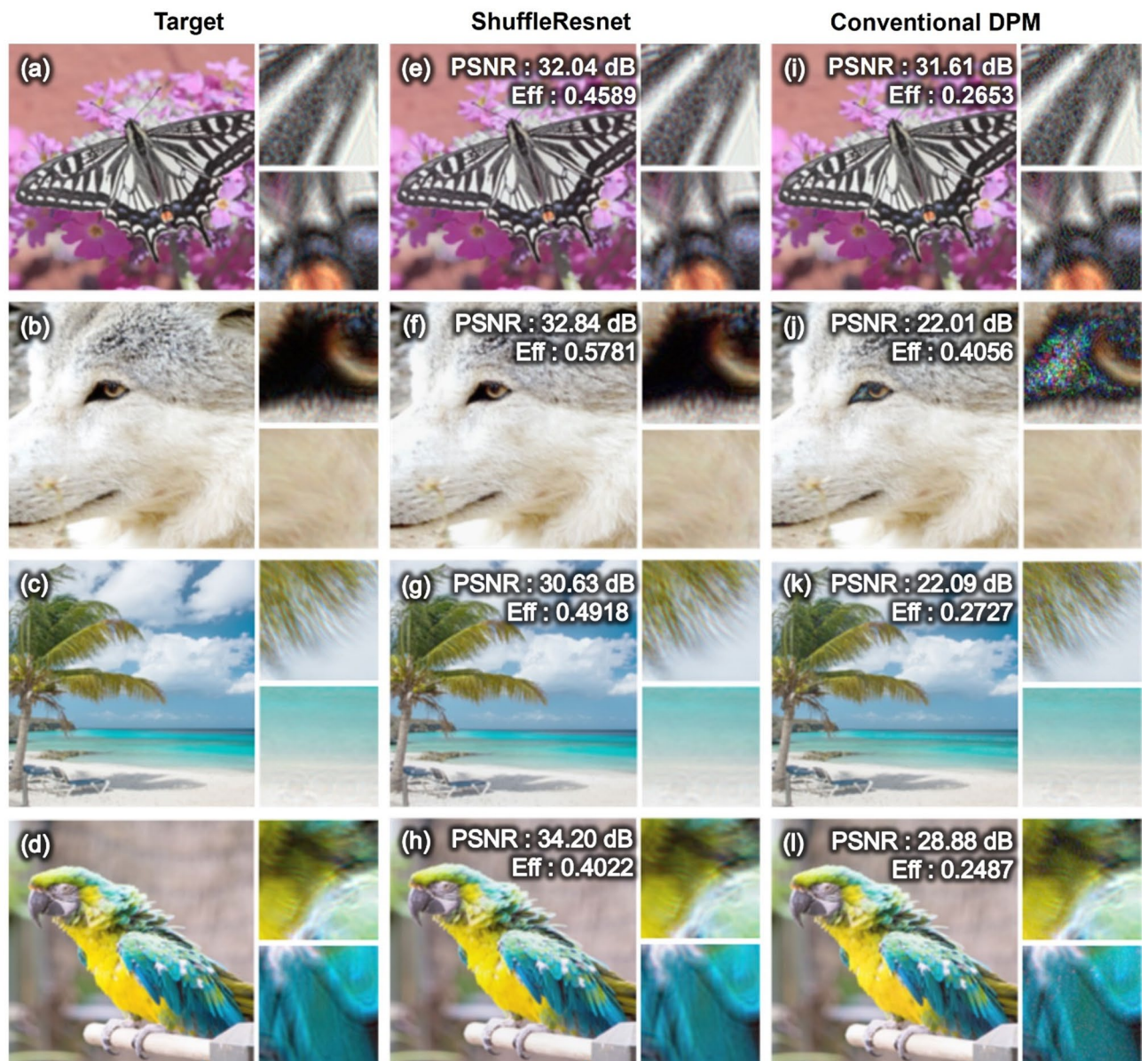


Fig. 4. Numerical reconstruction results of the complex field, compared with the original CGH as the target. Target CGHs (a–d), numerically reconstructed holograms from ShuffleResnet (e–h), and numerically reconstructed holograms from conventional DPM (i–l) are presented with their PSNR and optical efficiency values.

produced by ShuffleResnet achieves a well-structured checkerboard pattern, clearly preserved in the magnified region in the yellow box. This consistent pattern indicates stable and accurate encoding of phase information. The corresponding reconstruction in Fig. 5b achieves a high PSNR of 32.1dB and SSIM of 0.948. In contrast, Fig. 5c shows the encoded output generated by the conventional DPM, where the checkerboard structure appears irregular and disrupted in the zoomed region of the red box, it appears disrupted in the zoomed region of the red box, especially near textured or low-contrast regions of the image. As a result, the reconstruction in Fig. 5d exhibits high frequency artifacts, particularly in the background and low-contrast areas. These limitations are quantitatively reflected in the significantly lower PSNR of 9.01 dB and SSIM of 0.561.

Hyper-parameter tuning results

Light efficiency plays a crucial role in hologram reconstruction. By analyzing different efficiency ratios β , we observed a trade-off between light efficiency and reconstruction quality. Although a higher efficiency ratio increases light efficiency up to 0.9994, it also leads to a reduction in PSNR, which negatively impacts reconstruction quality.

Figure 6 illustrates the variation of light efficiency and PSNR as a function of efficiency ratios β . At lower efficiency ratios, the model achieves optimal reconstruction performance, with maximum PSNR and high light

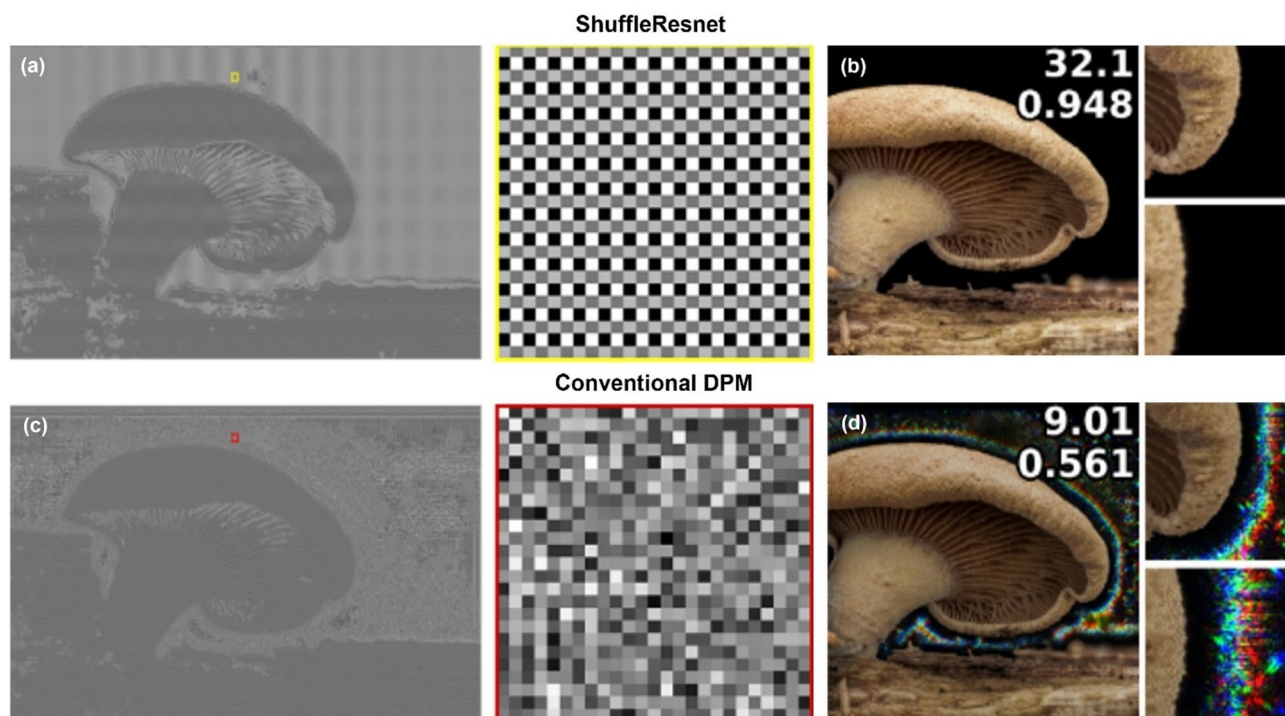


Fig. 5. Comparison of encoded output and reconstructed intensity between ShuffleResnet and conventional DPM. (a) Phase of ShuffleResnet output with yellow box indicating region of interest and corresponding zoomed-in view. (b) Corresponding reconstructed intensity with PSNR and SSIM metrics. (c) Phase of conventional DPM output with red box indicating region of interest and corresponding zoomed-in view. (d) Corresponding reconstructed intensity demonstrating the high frequency noise.

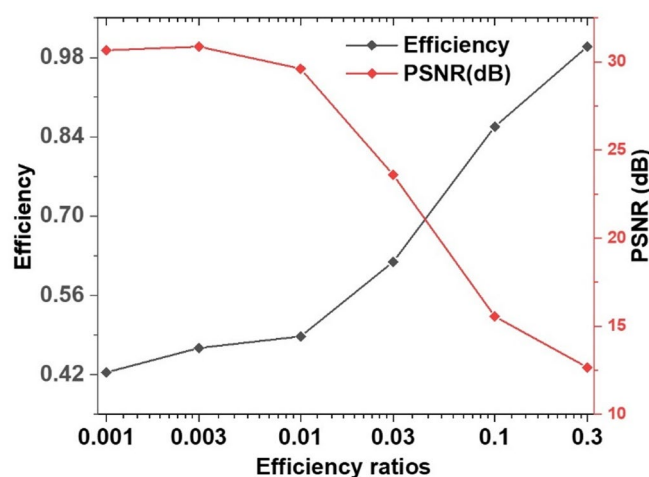


Fig. 6. Trade-off analysis between reconstruction quality (PSNR) and light efficiency at varying efficiency ratios β . Increasing β enhances the light efficiency but reduces reconstruction quality.

efficiency. As the efficiency ratio increases, light efficiency improves, but reconstruction quality decreases. For instance, at the highest ratio, efficiency reaches 0.9994, but the PSNR drops significantly to 12.66 dB. These results highlight a clear inverse relationship between PSNR and light efficiency.

Intensity-field comparison results

While Fig. 4 evaluated the complex field reconstruction quality at the SLM plane, Fig. 7 presents the simulated optical reconstruction results after propagation to a fixed observation plane for intensity-field comparison. The encoded holograms were numerically propagated using the ASM at a distance of 5 mm. Each image is annotated with its corresponding image quality metrics, such as PSNR and SSIM values. Compared to the

conventional DPM, the ShuffleResnet reconstructions appear closer to the targets, with high PSNR and SSIM. The reconstructed output from ShuffleResnet demonstrates enhanced light efficiency and reconstruction quality.

Table 1 summarizes the average PSNR, SSIM, and light efficiency values for both ShuffleResnet and the conventional DPM using 100 images from the DIV2K validation dataset. Overall, the proposed model ShuffleResnet yields a 0.75 dB increase in PSNR, indicating improved reconstruction fidelity. The SSIM improves by 4.2% reflecting better structural similarity to the target intensity field. Most notably, light efficiency increases by 59%, showing that a significantly larger portion of light contributes to the final image. These improvements collectively demonstrate the enhanced reconstruction quality and improved light efficiency, making it more suitable for real-world holographic display applications.

Experiment results

To validate the simulation results, we conducted experimental reconstructions. In our experiment, we first generated a 2D floating hologram, as in the simulation. Then we performed encoding using both the conventional DPM and our ShuffleResNet model, and experimentally reconstructed the hologram. We reconstructed the hologram using only the red channel and a red laser to simplify the experiment. To evaluate the light efficiency of the methods, we defined the relative efficiency as the ratio of the total intensity, defined as the sum of all

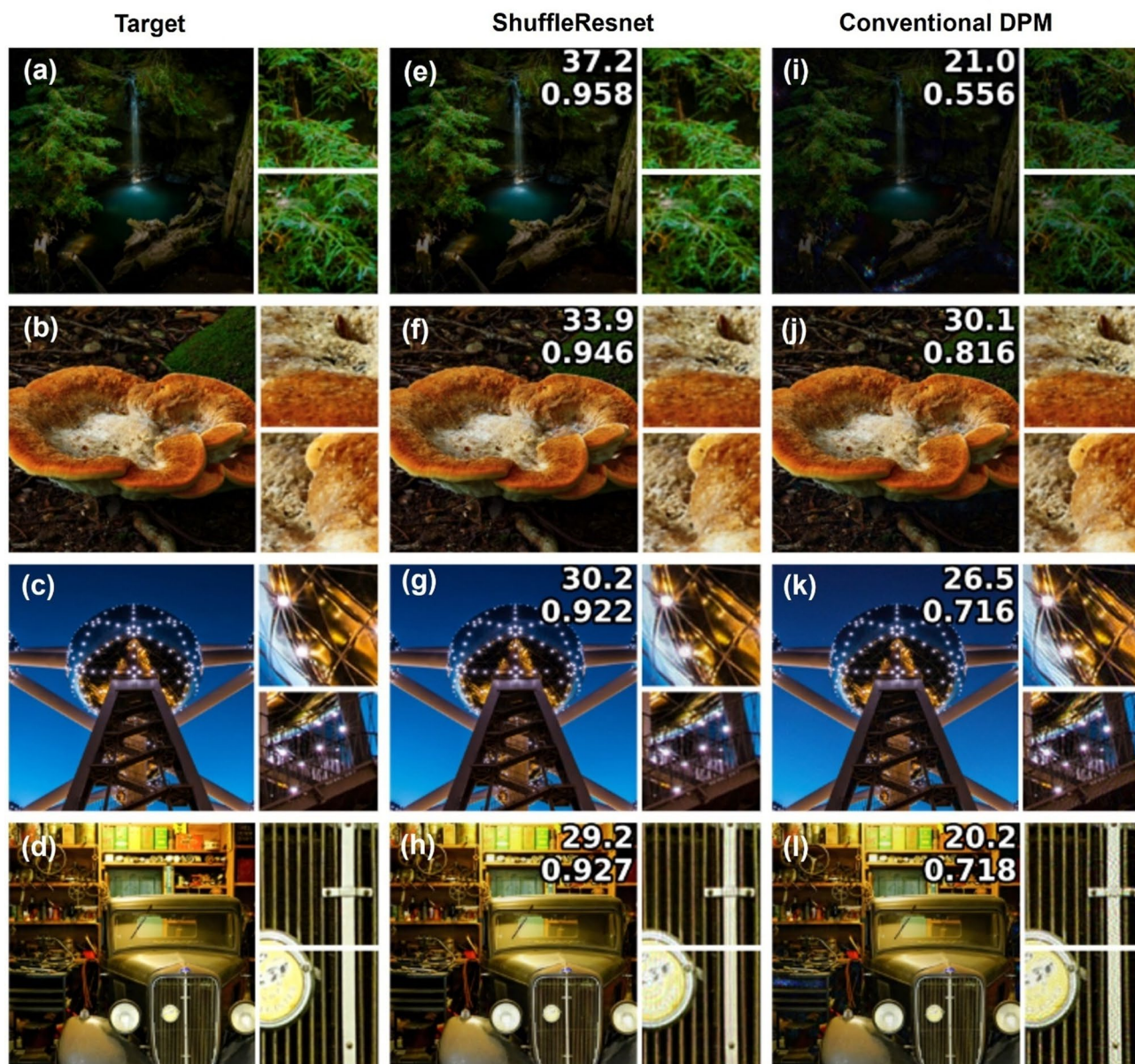


Fig. 7. Numerical reconstruction results after propagation for intensity-field representation. (a–d) Target ground-truth images from DIV2K validation dataset. (e–h) Numerically reconstructed holograms from ShuffleResnet. (i–l) corresponding reconstructions from the conventional DPM. Each output is annotated with PSNR and SSIM.

	Conventional DPM	ShuffleResnet
PSNR	27.36	28.11
SSIM	0.8729	0.9095
Efficiency	0.2764	0.4405

Table 1. Evaluation metrics of ShuffleResnet and conventional method based on the 100 images in the validation dataset for intensity field calculation.

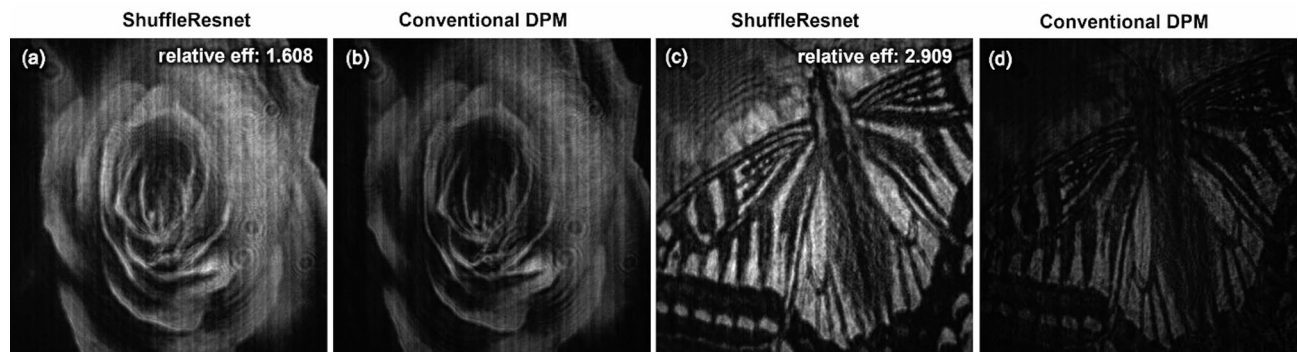


Fig. 8. Comparison of experimental results between ShuffleResnet (a,c) and conventional DPM (b,d). The relative optical efficiency of ShuffleResnet result, compared to the conventional DPM result, is indicated in the figure.

pixel values of the reconstructed image produced by ShuffleResnet, to that of the DPM output under identical conditions. This metric quantifies how much brighter the reconstruction is when using our encoding approach.

As shown in Fig. 8, although the image quality remains visually similar between both methods, the ShuffleResnet significantly improves light throughput efficiency. In Fig. 8a, ShuffleResnet achieves a relative efficiency of 1.608, while in Fig. 8c, the ShuffleResnet achieves 2.909 compared to conventional DPM. These results clearly confirm that the ShuffleResnet model achieves a substantial increase in light efficiency over the conventional approach.

Discussion and conclusion

While an end-to-end model that directly generates a phase-only hologram from a target image offers advantages in terms of application simplicity, our approach of decoupling the generation of the complex field from its encoding provides significant advantages in flexibility and modularity. Many computational holography algorithms first compute a complex field to address specific challenges before encoding it for display. For instance, sophisticated methods have been developed to enhance depth representation³³ or to expand the display eyebox³⁴. By implementing only the encoding stage, our method provides compatibility with such high-performance algorithms.

In this study, we introduced a model, ShuffleResnet, designed to enhance the reconstruction quality and light efficiency of double phase encoded holograms. Numerical simulation results demonstrate that the proposed model achieves higher quality of reconstructed holograms compared to conventional methods. The model significantly reduces the artifacts and increases the light efficiency of reconstructed holograms. Compared to conventional DPM, ShuffleResnet achieves a 59% increase in light efficiency without compromising reconstruction quality, making it well-suited for real-time holographic applications.

Methods

Network training and architecture

The overall framework consists of hologram generation, conventional double phase encoding for supervision, model training and evaluation. In our training pipeline, the ShuffleResnet model is trained on complex-valued holograms generated at random propagation depths to promote generalization in learning wavefront propagation. The actual propagation depth for each image is randomly selected as:

$$z = \frac{z_{base} \times \text{rand}(1, N)}{N} \quad (9)$$

Where z_{base} is the base propagation depth, $\text{rand}(1, N)$ selects a random integer from 1 to N , and N is number of depth levels considered. Once the propagation depth is determined, the complex wavefield is generated using the ASM, which simulates wave propagation in free space.

The initial wave field $U(x, y)$ is first transformed into the spatial frequency domain:

$$U(f_x, f_y) = \mathcal{F}\{U(x, y)\} \quad (10)$$

Where \mathcal{F} denotes the Fourier transform, $U(x, y)$ is the input complex field at the initial plane, $U(f_x, f_y)$ is the Fourier domain representation, which describes the spatial frequency components of the wavefront. The wavefield is propagated at depth Z by multiplying it with a phase term in the frequency domain as:

$$U(f_x, f_y, z) = U(f_x, f_y) \cdot e^{jk_z z} \quad (11)$$

Where k_z is the propagation term, defined by:

$$k_z = \sqrt{k^2 - (2\pi f_x)^2 - (2\pi f_y)^2} \quad (12)$$

With $k = \frac{2\pi}{\lambda}$ as the wave number. (f_x, f_y) denoting the spatial frequency coordinates. The propagated wavefield is transformed back into the spatial domain using the inverse Fourier transform given by:

$$U(x, y, z) = \mathcal{F}^{-1}\{U(f_x, f_y, z)\} \quad (13)$$

Where \mathcal{F}^{-1} is inverse Fourier Transform, $U(x, y, z)$ is the propagated complex field at depth z .

The generated CGH is encoded using conventional DPM which serves as the supervised training target. The real and imaginary components of the complex-valued holograms are separated and concatenated as input channels for the model. These holograms undergo pixel unshuffling operations as followed by residual blocks³⁵ and pixel shuffling³⁶ operations as shown in Fig. 9. The double-phase encoding method arranges two phase components (θ_1 and θ_2) in alternating pixels forming a checkerboard pattern. Standard convolutional neural networks apply uniform operations across all pixels, which is inefficient for this alternating structure where adjacent pixels represent different phase types. Pixel shuffling operations address this limitation by reorganizing the checkerboard pattern into separate channels, enabling independent processing of θ_1 and θ_2 components before reconstructing the spatial arrangement required for SLM display.

The Pixel Unshuffling operation increases the number of channels while reducing the spatial resolution by a Pixel shuffle factor (r). This transformation rearranges spatial information into separate feature channels, making it easier for convolutional layers to extract meaningful representations.

$$(B, C, H, W) \rightarrow \left(B, C \times r^2, \frac{H}{r}, \frac{W}{r}\right) \quad (14)$$

The Resnet Blocks consist of multiple stacked residual layers, each containing two (3×3) convolutional layers, followed by Batch Normalization and ReLU activation. This skip connection ensures stable gradient flow and prevents vanishing gradient issues. The residual unit can be represented by:

$$H(X) = F(X) + X \quad (15)$$

Where $F(X)$ represents the convolutional transformation applied to the input X . The final activation function used in ShuffleResnet is Hardtanh, which constrains the output values within a fixed range. The Pixel Shuffling operation restores the spatial resolution while reducing the number of channels, effectively reconstructing the output. The transformation is:

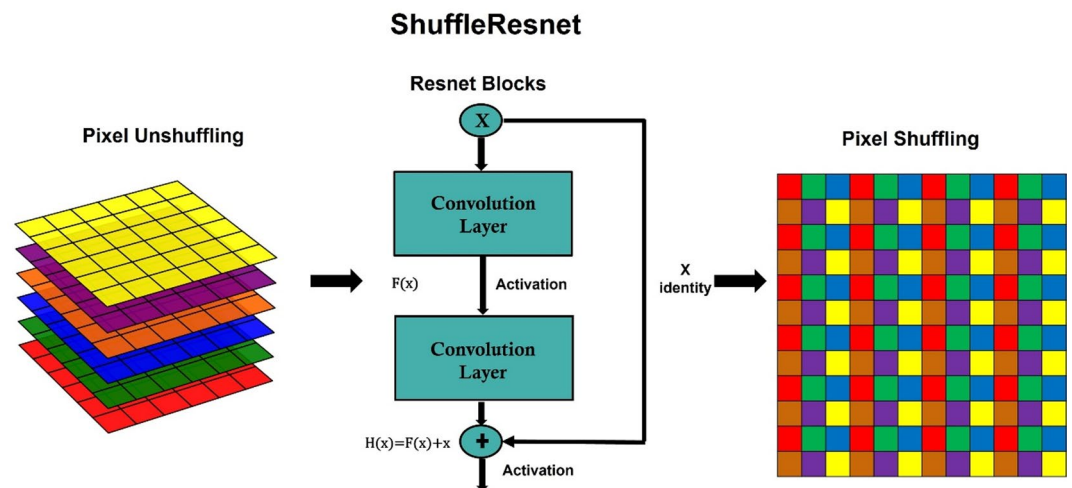


Fig. 9. The schematic model architecture of ShuffleResnet. The model ShuffleResnet contains pixel unshuffling operation as the first followed by Resnet blocks in the middle, and pixel shuffling operation as the final stage.

z (mm)	-10	-20	-30	-40	-50	-60	-70	-80
PSNR (dB)	30.47	30.99	30.28	30.86	30.22	30.78	30.47	30.30
Efficiency	0.4677	0.4555	0.4699	0.4671	0.4654	0.4376	0.4406	0.4592

Table 2. Validation results performance of ShuffleResnet across various distances for complex field in terms of PSNR and light efficiency.

Components	PSNR (dB)	Efficiency
ShuffleResnet	30.47	0.4677
w/o pixel shuffle	23.08	0.4954
w/o unsupervised loss	22.53	0.2764

Table 3. Ablation study results for individual components on reconstruction quality and light efficiency.

$$\left(B, C \times r^2, \frac{H}{r}, \frac{W}{r}\right) \rightarrow (B, C, H, W) \tag{16}$$

The training dataset contains 800 images in DIV2K dataset, which consists of high-resolution natural images. Each image is resized to 1080×1920 pixels and converted into a complex-valued hologram. To enhance generalization, a random propagation depth is assigned for each sample. The base propagation z_{base} is taken as 40 mm and $N = 8$ represents the number of discrete propagation depths. The complex hologram is separated into real and imaginary components, which are concatenated along the channel dimension to form the input to the model. These holograms undergo pixel unshuffling to rearrange spatial information before being processed by Resnet blocks, after which pixel shuffling restores the spatial arrangement while preserving phase structure. The model is trained for 400 epochs using Adam optimizer with a learning rate of 0.0001, and a batch size of 1. The training time for the model is 25 h. For validation, we use DIV2K validation dataset, which contains 100 images. In this case, the fixed depth of -10 mm was used to generate the hologram input. The reconstruction was performed in the SLM plane using ASM. A band-limiting optical filter was applied during the simulation to reduce diffraction noise. Finally, the reconstructed output was propagated to 5 mm to get the final intensity-field representations, simulating the output seen on a real optical display.

Validation results across various distances

Table 2 shows the validation performance of proposed model across various distances for complex field in terms of PSNR and light efficiency using 100 images from the DIV2K validation dataset. The results demonstrate that reconstruction quality shows minimal dependency on propagation distance, with PSNR values remaining within a narrow range of ±0.8 dB and efficiency values stable around 0.44–0.47, confirming the model’s robust generalization across different depths.

Ablation study results

To validate the contribution of each proposed component in ShuffleResnet, we conducted systematic ablation experiments by removing key architectural elements and training objectives. Table 3 summarizes the ablation study results, demonstrating the impact of individual components on reconstruction quality and light efficiency for complex field.

The removal of pixel shuffle and unshuffle operations yielded a PSNR decrease of 7.39 dB, illustrating their critical role in managing the complex spatial structure of double phase encoding. While the efficiency slightly increased to 0.4954 in this configuration, this improvement came at the severe cost of reconstruction quality. Elimination of the unsupervised reconstruction loss produced an even more substantial performance degradation, with PSNR decreasing by 7.94 dB and efficiency declining to 0.2764, performing lower than conventional DPM. These results indicate that the reconstruction loss constitutes the primary mechanism driving both quality enhancement and efficiency improvement, as it optimizes the network to generate clean, artifact-free holograms from the original complex field rather than replicating conventional DPM patterns.

Experimental setup

Our experimental setup consists of a 638 nm red laser, a phase-only SLM, a 4-f imaging system, and a camera to capture the reconstructed hologram. The phase-only hologram, generated by either the ShuffleResnet model or the conventional DPM method, is uploaded onto the SLM. The collimated laser beam illuminates the SLM, modulating the wavefront based on the encoded phase. The modulated light is then relayed through a 4-f system to remove the undesired patterns, and the resulting reconstructed field is recorded by a CMOS camera placed at a propagation distance of −60 mm from the SLM plane. The captured intensity data is used to assess light efficiency by computing the sum of pixel intensities in the red channel.

Data availability

The data that support the findings of this study are available from the corresponding author upon reasonable request.

Received: 26 June 2025; Accepted: 9 September 2025

Published online: 13 October 2025

References

- Gabor, D. A., New microscopic & principle *Nature* **161** (4098), 777–778. <https://doi.org/10.1038/161777a0>. (1948).
- Gabor, D. Microscopy by reconstructed wave fronts: II. *Proc. Phys. Soc. B.* **64** (6), 449–469. <https://doi.org/10.1088/0370-1301/64/6/301> (1951).
- Reconstructed Wavefronts and Communication Theory**. (accessed 12 March 2025); <https://opg.optica.org/viewmedia.cfm?r=1&rwjcode=josa&uri=josa-52-10-1123&html=true>
- Lohmann, A. W. & Paris, D. P. Binary Fraunhofer holograms, generated by computer. *Appl. Opt. AO.* **6** (10), 1739–1748. <https://doi.org/10.1364/AO.6.001739> (1967).
- Brown, B. R. & Lohmann, A. W. Complex Spatial filtering with binary masks. *Appl. Opt. AO.* **5** (6), 967–969. <https://doi.org/10.1364/AO.5.000967> (1966).
- Paturzo, M. et al. Synthesis and display of dynamic holographic 3D scenes with Real-World objects. *Opt. Express OE.* **18** (9), 8806–8815. <https://doi.org/10.1364/OE.18.008806> (2010).
- Kozacki, T., Kujawińska, M., Finke, G., Hennelly, B. & Pandey, N. Extended viewing angle holographic display system with Tilted SLMs in a circular configuration. *Appl. Opt. AO.* **51** (11), 1771–1780. <https://doi.org/10.1364/AO.51.001771> (2012).
- Pi, D., Liu, J. & Wang, Y. Review of Computer-Generated hologram algorithms for color dynamic holographic Three-Dimensional display. *Light Sci. Appl.* **11** (1), 231. <https://doi.org/10.1038/s41377-022-00916-3> (2022).
- Chu, J. C. H. et al. Application of holographic display in radiotherapy treatment planning II: A Multi-Institutional study. *J. Appl. Clin. Med. Phys.* **10** (3), 115–124. <https://doi.org/10.1120/jacmp.v10i3.2902> (2009).
- Abdelazeem, R. M., Youssef, D., El-Azab, J., Hassab-Elnaby, S. & Agour, M. Three-Dimensional visualization of brain tumor progression based accurate segmentation via comparative holographic projection. *PLOS One* **15** (7), e0236835. <https://doi.org/10.1371/journal.pone.0236835> (2020).
- Bauchert, K. A., Serati, S. A., Sharp, G. D., McKnight, D. J. & SPIE. Complex phase/amplitude spatial light modulator advances and use in a multispectral optical correlator. In *Optical Pattern Recognition VIII* Vol. 3073, pp 170–177. <https://doi.org/10.1117/12.270361> (1997).
- Tsang, P. W. M. *Computer-Generated Phase-Only Holograms for 3D Displays: A Matlab Approach* (Cambridge University Press, 2021).
- Liu, K., He, Z. & Cao, L. Double amplitude freedom Gerchberg–Saxton algorithm for generation of Phase-Only hologram with speckle suppression. *Appl. Phys. Lett.* **120** (6), 061103. <https://doi.org/10.1063/5.0080797> (2022).
- Chang, C. et al. Speckle-Suppressed Phase-Only holographic Three-Dimensional display based on Double-Constraint Gerchberg–Saxton algorithm. *Appl. Opt. AO.* **54** (23), 6994–7001. <https://doi.org/10.1364/AO.54.006994> (2015).
- Wu, Y. et al. Adaptive weighted Gerchberg–Saxton algorithm for generation of Phase-Only hologram with artifacts suppression. *Opt. Express OE.* **29** (2), 1412–1427. <https://doi.org/10.1364/OE.413723> (2021).
- Chen, C. et al. Multi-Depth hologram generation using stochastic gradient descent algorithm with complex loss function. *Opt. Express OE.* **29** (10), 15089–15103. <https://doi.org/10.1364/OE.425077> (2021).
- Peng, Y., Choi, S., Kim, J. & Wetzstein, G. Speckle-Free holography with partially coherent light sources and Camera-in-the-Loop calibration. *Sci. Adv.* **7** (46), eabg5040. <https://doi.org/10.1126/sciadv.abg5040> (2021).
- Liu, S. & Takaki, Y. Gradient descent based algorithm of generating Phase-Only holograms of 3D images. *Opt. Express OE.* **30** (10), 17416–17436. <https://doi.org/10.1364/OE.449969> (2022).
- Tsang, P. W. M. & Poon, T. C. Novel method for converting digital Fresnel hologram to Phase-Only hologram based on bidirectional error diffusion. *Opt. Express OE.* **21** (20), 23680–23686. <https://doi.org/10.1364/OE.21.023680> (2013).
- Tsang, P. W. M., Chow, Y. T. & Poon, T. C. Generation of Phase-Only Fresnel hologram based on down-Sampling. *Opt. Express OE.* **22** (21), 25208–25214. <https://doi.org/10.1364/OE.22.025208> (2014).
- Mendoza-Yero, O., Mínguez-Vega, G. & Lancis, J. Encoding complex fields by using a Phase-Only optical element. *Opt. Lett.* **39** (7), 1740. <https://doi.org/10.1364/OL.39.001740> (2014).
- Zea, A. V., Ramirez, J. F. B. & Torroba, R. Optimized random phase only holograms. *Opt. Lett. OL.* **43** (4), 731–734. <https://doi.org/10.1364/OL.43.000731> (2018).
- Shi, L., Li, B., Kim, C., Kellnhofer, P. & Matusik, W. Towards Real-Time photorealistic 3D holography with deep neural networks. *Nature* **591** (7849), 234–239. <https://doi.org/10.1038/s41586-020-03152-0> (2021).
- Shi, L., Li, B. & Matusik, W. End-to-End learning of 3D Phase-Only holograms for holographic display. *Light Sci. Appl.* **11** (1), 247. <https://doi.org/10.1038/s41377-022-00894-6> (2022).
- Hsueh, C. K. & Sawchuk, A. A. Computer-Generated Double-Phase holograms. *Appl. Opt. AO.* **17** (24), 3874–3883. <https://doi.org/10.1364/AO.17.003874> (1978).
- Arrizón, V. & Sánchez-de-la-Llave, D. Double-Phase holograms implemented with Phase-Only Spatial light modulators: performance evaluation and improvement. *Appl. Opt. AO.* **41** (17), 3436–3447. <https://doi.org/10.1364/AO.41.003436> (2002).
- Song, H. et al. Optimal synthesis of Double-Phase computer generated holograms using a Phase-Only Spatial light modulator with grating filter. *Opt. Express OE.* **20** (28), 29844–29853. <https://doi.org/10.1364/OE.20.029844> (2012).
- Kim, Y. K., Lee, J. S. & Won, Y. H. Low-Noise High-Efficiency Double-Phase hologram by multiplying a weight factor. *Opt. Lett. OL.* **44** (15), 3649–3652. <https://doi.org/10.1364/OL.44.003649> (2019).
- Sui, X. et al. Spatiotemporal Double-Phase hologram for Complex-Amplitude holographic displays. *Chin. Opt. Lett.* **18** (10), 100901. <https://doi.org/10.3788/COL202018.100901> (2020).
- Zhong, C. et al. Real-Time 4K Computer-Generated hologram based on encoding conventional neural network with learned layered phase. *Sci. Rep.* **13** (1), 19372. <https://doi.org/10.1038/s41598-023-46575-1> (2023).
- Yan, X. et al. Recoding Double-Phase holograms with the full convolutional neural network. *Opt. Laser Technol.* **174**, 110667. <https://doi.org/10.1016/j.optlastec.2024.110667> (2024).
- Maimone, A., Georgiou, A. & Kollin, J. S. Holographic Near-Eye displays for virtual and augmented reality. *ACM Trans. Graph.* **36** (4), 1–16. <https://doi.org/10.1145/3072959.3073624> (2017).
- Yang, D. et al. Diffraction-Engineered holography: beyond the depth representation limit of holographic displays. *Nat. Commun.* **13** (1), 6012. <https://doi.org/10.1038/s41467-022-33728-5> (2022).
- Chang, C., Cui, W., Park, J. & Gao, L. Computational holographic maxwellian Near-Eye display with an expanded eyepiece. *Sci. Rep.* **9** (1), 18749. <https://doi.org/10.1038/s41598-019-55346-w> (2019).
- He, K., Zhang, X., Ren, S. & Sun, J. Deep residual learning for image recognition. *ArXiv* **10** <https://doi.org/10.48550/arXiv.1512.03385> (2015).

36. Shi, W. et al. Real-time single image and video super-resolution using an efficient sub-pixel convolutional neural network. *ArXiv* <https://doi.org/10.48550/arXiv.1609.05158> (2016).

Acknowledgements

This work was supported by the National Research Foundation of Korea (NRF) grant funded by the Korean government (MSIT) (No. RS-2023-00245184 and RS-2024-00341142).

Author contributions

B.P. and D.Y. conceived the idea and wrote the manuscript. H.H did the experiment. D.Y. supervised the project.

Declarations

Competing interests

The authors declare no competing interests.

Additional information

Correspondence and requests for materials should be addressed to D.Y.

Reprints and permissions information is available at www.nature.com/reprints.

Publisher's note Springer Nature remains neutral with regard to jurisdictional claims in published maps and institutional affiliations.

Open Access This article is licensed under a Creative Commons Attribution-NonCommercial-NoDerivatives 4.0 International License, which permits any non-commercial use, sharing, distribution and reproduction in any medium or format, as long as you give appropriate credit to the original author(s) and the source, provide a link to the Creative Commons licence, and indicate if you modified the licensed material. You do not have permission under this licence to share adapted material derived from this article or parts of it. The images or other third party material in this article are included in the article's Creative Commons licence, unless indicated otherwise in a credit line to the material. If material is not included in the article's Creative Commons licence and your intended use is not permitted by statutory regulation or exceeds the permitted use, you will need to obtain permission directly from the copyright holder. To view a copy of this licence, visit <http://creativecommons.org/licenses/by-nc-nd/4.0/>.

© The Author(s) 2025